

Mechanical Tension of Biomembranes Can Be Measured by Super Resolution (STED) Microscopy of Force-Induced Nanotubes

Debjit Roy, Jan Steinkühler, Ziliang Zhao, Reinhard Lipowsky, and Rumiana Dimova*

Cite This: *Nano Lett.* 2020, 20, 3185–3191

Read Online

ACCESS |

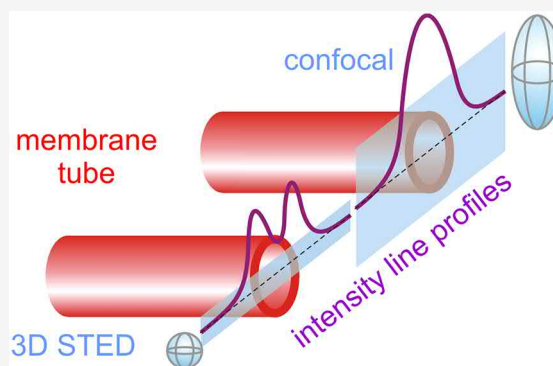
Metrics & More

Article Recommendations

Supporting Information

ABSTRACT: Membrane tension modulates the morphology of plasma-membrane tubular protrusions in cells but is difficult to measure. Here, we propose to use microscopy imaging to assess the membrane tension. We report direct measurement of membrane nanotube diameters with unprecedented resolution using stimulated emission depletion (STED) microscopy. For this purpose, we integrated an optical tweezers setup in a commercial microscope equipped for STED imaging and established micropipette aspiration of giant vesicles. Membrane nanotubes were pulled from the vesicles at specific membrane tension imposed by the aspiration pipet. Tube diameters calculated from the applied tension using the membrane curvature elasticity model are in excellent agreement with data measured directly with STED. Our approach can be extended to cellular membranes and will then allow us to estimate the mechanical membrane tension within the force-induced nanotubes.

KEYWORDS: giant vesicles, membrane nanotubes, STED microscopy, micropipette aspiration, membrane tension, optical tweezers



INTRODUCTION

Cellular membranes are found to attain a multitude of morphologies and often exhibit highly curved segments with certain functionality. In particular, highly curved membrane nanotubes are involved in several cellular functions such as cell migration,¹ signaling,² remote communication and motility,³ and cell spreading.⁴ Tunneling membrane nanotubes also play an important role in transfer of cellular content (small molecules, proteins, prions, viral particles, vesicles, and organelles) in a variety of cell types^{5–9} as well as electrical signals.¹⁰ During migration, tubular membrane protrusions (also referred to as retracting fibers) are formed behind the migrating cell and are responsible for releasing cellular content.¹¹ In all of these examples, when not supported by the underlying substrate, membrane shape is modulated by membrane tension which affects the membrane surface area and morphology.^{12,13} Membrane tension thus provides a link between membrane mechanics, morphology, as well as mechanical transduction in the cell, for example, via tension-sensitive membrane channels. However, how cellular tension is regulated and mechanobiological cues are perceived by the cell is poorly understood.¹⁴

In principle, plasma membrane tension can be indirectly inferred from nanotube pulling experiments where the membrane diameter and force of pulling could be used to extract membrane mechanical parameters such as tension, bending rigidity, and spontaneous curvature.^{15–19} Tension-sensitive probes with fluorescence decay lifetimes depending

on tension have also been recently introduced.²⁰ However, it is unclear how curvature and local probe concentration increase due to sorting mechanisms affects the dye performance. Apart from providing the means to assess the membrane bending rigidity and tension, tube pulling experiments also allow the study of cellular processes that take place at highly curved membranes.^{21–26} In these experiments, the cell or vesicle is immobilized or more often aspirated by a micropipette setting the membrane tension, and a tube is typically pulled by means of optical-tweezer manipulation of a bead attached to the membrane. For a fixed bending rigidity of the membrane, the tube radius depends on membrane tension and thus measuring the radius allows assessing this mechanical parameter. However, membrane nanotube diameters are not directly accessible via diffraction-limited microscopy imaging and these limitations obstruct progress in the field.²⁷

Here, we measure for the first time the diameter of membrane nanotubes directly using stimulated emission depletion (STED) nanoscopy as a function of membrane tension in a controlled reconstituted system. To form membrane nanotubes, we employ giant unilamellar lipid

Received: December 20, 2019

Revised: April 20, 2020

Published: April 22, 2020



vesicles (GUVs).²⁸ GUVs represent a popular model system of cellular membranes as their response to external factors as well as thermodynamic state can be visualized under the optical microscope.^{29,30} In addition, they are amenable to micromanipulation (see Chapters 11 and 16 of ref 28). Pulling a membrane nanotube (also referred to as tether) provides such a micromanipulation protocol, in which a cylindrical membrane segment with a diameter ranging between 20 nm to few hundreds nanometers is extruded from the GUV. Controlled membrane nanotubes can be generated by hydrodynamic flow^{31–34} (both inward and outward tubes with respect to the vesicle body can be pulled³⁴), gravity,³⁵ micromanipulation,^{31,36,37} and magnetic or optical tweezers^{15,38–40} (see also overview in ref 41), whereby tube formation is enforced by a localized pulling force.

We use micropipettes to aspirate and hold the vesicle in place and to modulate the membrane tension by adjusting the aspiration pressure. The imposed tension mimics cellular conditions corresponding to the cortical tension.⁴² To pull the nanotube from the vesicle, a sticky microsphere, trapped by the optical tweezers, is used as a handle. For a GUV being aspirated at a suction pressure, at which the GUV tongue inside the micropipette is longer than the micropipette radius, the total membrane tension is given by⁴¹

$$\hat{\Sigma} = \Delta P_{\text{asp}} \frac{R_v R_p}{2(R_v - R_p)} + 2\kappa m \left(\frac{1}{R_p} + \frac{1}{R_v} \right) \quad (1)$$

where R_v and R_p are the respective radius of the vesicle and micropipette, ΔP_{asp} is the aspiration pressure of the micropipette, m is the membrane spontaneous curvature, and κ is the bending rigidity of the membrane. The first term in eq 1 is the aspiration tension⁴³ for which we will use the notation Σ_{asp} . The trapped bead, located at the terminal of an outward nanotube pulled from the aspirated GUV, experiences a force^{13,41}

$$f_t = 2\pi\sqrt{2\kappa\hat{\Sigma}} - 4\pi\kappa m - \frac{\pi\kappa}{R_v} \quad (2)$$

which contains two terms that depend on the spontaneous curvature m , because the total membrane tension $\hat{\Sigma}$ depends on the spontaneous curvature as well, see eq 1. In our experiments, the spontaneous curvature is so small that we can ignore these two m -dependent terms; further below, we will justify this condition for the system we explore. As a consequence, the total membrane tension $\hat{\Sigma}$ reduces to the first term in eq 1, which represents the aspiration tension Σ_{asp} . Furthermore, for negligible spontaneous curvature, the aspiration tension becomes equal to the mechanical tension which can now be deduced from the aspiration geometry and the aspiration pressure. In addition, the last term in eq 2 can be ignored because of the small mean curvature of the vesicle.

To perform tube pulling experiments, we switch between confocal fluorescence and bright-field imaging: the membrane nanotube is visualized in confocal mode and the force on the trapped object is obtained from bead position recorded in bright-field mode. At a fixed tube length, the force f_v acting on the trapped bead, can be estimated from the bead off-center displacement from the trap axis, Δx , as $f_t = \kappa_{\text{tr}} \Delta x$, where κ_{tr} is the trap constant determined independently, see [Experimental Section](#). From the dependence f_t versus $\sqrt{\Sigma_{\text{asp}}}$, one can deduce the bending rigidity. Alternatively, this material property could

be assessed from the membrane nanotube radius, if the latter could be measured: the radius of a cylindrical tube R_t depends on the aspiration tension through the relation^{41,44}

$$R_t = \sqrt{\frac{\kappa}{2\Sigma_{\text{asp}}}} \quad (3)$$

In general, the tube radius is smaller than the resolution of the optical microscope (~ 200 nm), which makes it impossible to measure it directly. AFM imaging could be used when the tubes adhere to a substrate⁴⁵ but, as a result of this adhesion, the tube morphology will be deformed into a noncylindrical shape which can no longer be described by the tube radius alone. In other studies, the tube radius is estimated indirectly from correlating the fluorescence intensity count.^{46–48} However, it is unclear how curvature influences the dye performance. Moreover, dye sorting taking place in membrane nanotubes^{16,49} necessarily affects the tube fluorescence intensity and thus the measurement of the nanotube diameter. The radii of spontaneously formed tubes (not pulled by tweezers) can be also roughly inferred from spontaneous curvature measurements^{17,50,51} (see pages 9–11 in ref 52 for a review of approaches to measure the membrane spontaneous curvature), but an assumption has to be made for the shape of the tube (cylindrical or necklace-like).

With the advent of super resolution microscopy, the optical microscope resolution has been improved to a few tens of nanometers^{53,54} and thus, in principle, can be used to measure membrane nanotube diameters. Previously, STED microscopy has been used to study the membrane heterogeneity^{55–57} and to assess dimensions of endoplasmic reticulum structures using point spread function fitting.⁵⁸ It has advantages over other super resolution microscopic techniques such as photo-activated localization microscopy (PALM)⁵⁹ and stochastic optical reconstruction microscopy (STORM),⁶⁰ which require the acquisition of a high number of images (typically a few thousand frames)⁶¹ and are thus slower imaging techniques. In this Letter, we report direct measurement of membrane nanotube diameters with unprecedented resolution using STED microscopy. For this purpose, we have integrated an optical tweezers setup in a microscope equipped for STED imaging.

■ EXPERIMENTAL SECTION

Vesicle Preparation and Characterization. GUVs were grown from 1-palmitoyl-2-oleoyl-*sn*-glycero-3-phosphatidylcholine (POPC) doped with 0.1 mol % biotinyl cap phosphatidylethanolamine (PE) (both from Avanti Polar Lipids) and 0.5 mol % ATTO 647N dye (AttoTech) using electroformation in 100 mOsm/kg sucrose solution; for details see Section S1 in the [Supporting Information \(SI\)](#). Occasionally, we also explored vesicle membranes containing cholesterol (Chol), namely at POPC/Chol 9:1 molar ratio. An optically trapped streptavidin-coated bead of diameter ~ 2 μm adhered to the vesicles due to biotin–streptavidin bonding. The vesicles were diluted in isotonic medium of 40 mM glucose and 30 mM sodium chloride solution. This external solution was chosen (i) to enhance the optical contrast of the vesicle in phase-contrast observation but avoid vesicle deformation by gravity, (ii) to ensure strong biotin–streptavidin binding, which requires the presence of sodium chloride,⁴⁰ and (iii) to establish conditions of low asymmetry across the membrane so that the spontaneous curvature is negligible⁵¹ (at these

conditions the spontaneous curvature is comparable to the mean curvature of the GUVs and the last two terms in eq 2 can be ignored). The bending rigidity of the membrane was measured from fluctuation analysis according to previously published protocol,⁶² see Section S2 in the Supporting Information. All experiments were performed at ~ 22 °C. MATLAB (2014a) and Origin 2015 were used for the image and data analysis.

Experimental Setup. In our experiment, a membrane nanotube is extruded from an aspirated GUV using an optically trapped microsphere (Figure 1). The setup includes three parts

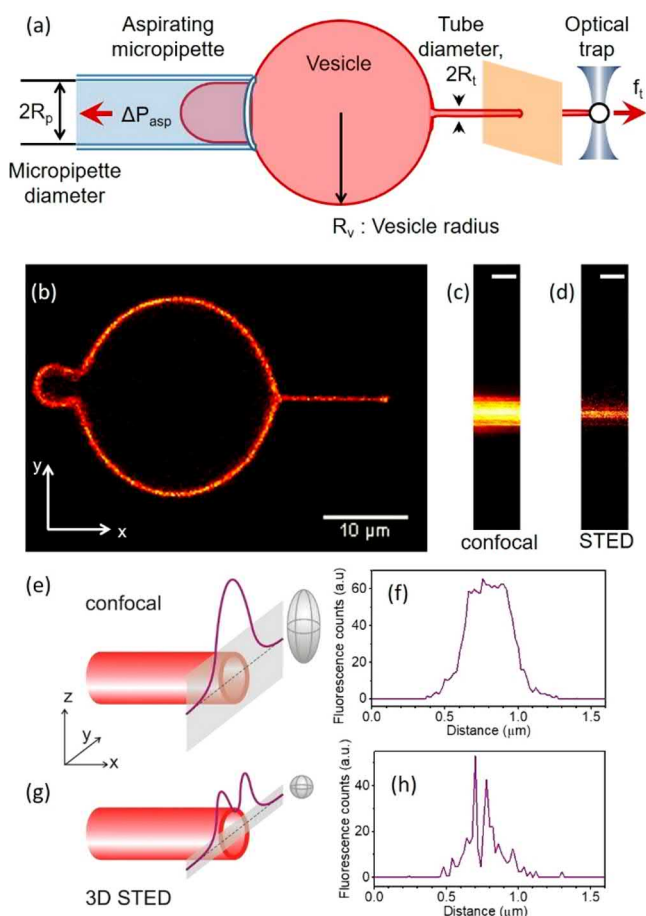


Figure 1. Scheme of the experimental approach of pulling membrane nanotubes and example line scans acquired with confocal and STED microscopy. (a) Schematic of the experiment. (b) Membrane nanotube extrusion as seen in confocal fluorescence imaging. (c) Confocal and (d) 3D STED image of a small portion of the extruded nanotube (scale bars correspond to 500 nm). (e, g) Schematic illustration and (f, h) experimentally acquired data from line scans (gray bands in panels e and g) across a membrane nanotube (red cylinder) when using confocal (e, f) and 3D STED (g, h) imaging; for lucidity, the rough dimensions of the scanning voxels are illustrated as gray ellipsoids in (e, g).

(see Section 3 in the SI): micropipette system to hold and aspirate GUVs, optical tweezers to extract the membrane nanotube, and confocal and STED scanning for fluorescence imaging. The setup is based on an inverted microscope (IX83, Olympus Inc., Japan), which is a part of a commercial STED system (Abberior GmbH, Germany). For optical trapping, we have established home-built tweezers by introducing a continuous wave TEM₀₀ mode 1064 nm laser beam (YLR-

10-LP, IPG Photonics Corp.) from the microscope back port (SI Figure S1). The laser beam is tightly focused using a 1.2 numerical aperture (NA) water immersion objective (UPLSA-PO60, Olympus Inc., Japan with a working distance of 0.28 mm) to form the optical trap. The objective is also used for the fluorescence imaging. Bright-field images were collected using a CCD camera positioned at the back port of the microscope (SI Figure S1). To quantify the trap stiffness, we employed the viscous drag method: the sample was displaced at a constant velocity while trapping a bead and monitoring its off-center displacement, see SI Section S3.1. To hold and aspirate the GUVs, a micropipette was inserted into the sample chamber using a three-dimensional micromanipulator system (Narishige Corp., Japan) clamped on the microscope (SI Section S3.2). For fluorescence imaging, a 640 nm pulsed laser was used for excitation and another pulsed 775 nm laser beam was used for emission depletion. A spatial light modulator placed in the STED beam path enabled 3D STED; for comparison between 2D and 3D STED, see SI Section S3.3).

RESULTS AND DISCUSSION

GUVs with diameters typically between ~ 20 to 25 μm were aspirated via micropipettes with diameters of 3 to 5 μm . A floppy GUV was chosen (see Movie S1 for an example), aspirated by the micropipette at a low aspiration pressure and brought into the contact with streptavidin-coated bead trapped by the optical tweezers. The low vesicle tension allowed us to achieve a larger contact area of the bead with the membrane (occasionally the vesicle was displaced so that the position of the bead was well inside the GUV interior but still engulfed by the membrane). After waiting for few seconds, the aspirated GUV was moved away from the trapped bead and a membrane nanotube was extruded from the vesicle due to strong biotin–streptavidin noncovalent bonding. In all experiments, we kept the length of the enforced nanotube to be between 8 and 10 μm . By doing so, the hydrodynamic contribution arising from the vesicle wall is minimized.⁶³ If the tube is shorter, not only the noncylindrical part of the vesicle and the fluorescence from it can affect the measurements but also the high power STED beam can destabilize the trapped bead and affect the trapping efficiency. Much longer tubes were also avoided as the whole GUV with its aspirated tongue would be out of the field of view. In addition, trapping potential in the outer region of the imaging field could be affected by spherical aberration of the microscope objective.

The membrane nanotube was visualized under the confocal microscope (Figure 1b). For the ease of the experiments, the center of the GUV spherical portion outside the pipet and the center of the trapped bead (and thus also the membrane nanotube) were kept in the same plane, which was fixed to 20 μm above of the cover glass surface; this condition ensured no hydrodynamic effects on the trapped bead and constant trapping efficiency.⁶³ The micropipette and GUV diameters were measured from the confocal image.

To measure the tube diameter, we recorded a kymograph of a line scan perpendicular to the nanotube axis (y -axis in Figure 1b). Even though the signal-to-noise (S/N) ratio of 2D STED images was higher than those of 3D STED images (see Figure S5 in the Supporting Information), the out-of-focus signal arising from the nanotube practically reduces the resolution in the former images. This effect is even more pronounced when comparing confocal and 3D STED scans, see Figure 1c–h. The pixel dwell time was adjusted to 20 μs to obtain 3D STED

images with significant S/N ratio and higher effective resolution compared to 2D STED imaging. The STED resolution was measured using 20 nm beads and found to be <40 nm in both x - and y -axes (SI Section S3.3 and Figures S3 and S4). Therefore, in a STED line scan across the tube, the two wall-crossings of a membrane nanotube with radius larger than 20 nm should be, in theory, resolvable under these system settings. However, due to the inherent vibrations of the micropipette (~ 31 nm, over six measurements of the positional fluctuations of the micropipette tip), the thermal motion of trapped beads (~ 15 nm, obtained from the trap stiffness, which was measured to be 74 ± 2 pN/ μm , see SI Section S3.1), and the GUV itself, the membrane nanotubes are found to laterally fluctuate with an amplitude of the order of few hundred nanometers in the y -direction (see Figure 2a,b), which is in the range of the expected tube diameter. As a

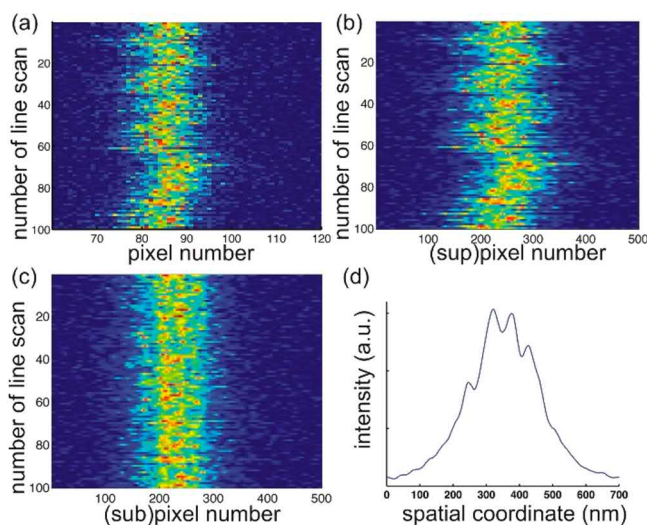


Figure 2. Tube line-scan kymograph, line-scans alignment and extraction of an averaged intensity profile. (a) A 3D STED kymograph consisting of 100 line scans of a single nanotube collected with 20 nm pixel size at 20 μs pixel dwell time (color code indicates intensity); the tube exhibits significant lateral fluctuations in the y -direction. (b) To obtain subpixel accuracy the individual line scans were linearly interpolated with 0.1 pixel resolution (see SI Section S4). (c) Same nanotube kymograph after alignment of the line scans according to maximal intensity overlap. (d) Averaged line scan along the y -axis of a single line-scan kymograph, which enables reliable detection of the nanotube diameter from the y -position position of the two highest maxima. This particular tube had a diameter of 72 ± 11 nm.

result, in a major fraction of the line scans in a kymograph, instead of two clearly defined peaks (as sketched in Figure 1g), we detect several noisy maxima. The appearance of multiple peaks was reduced to some extent by adjusting the pixel size to 20 nm (at lower pixel size, the scans were significantly noisier, see SI Figure S6). Larger pixel sizes were not explored as the resolution of the STED microscope was found to be <40 nm in both x - and y -axes while the pixel size is typically kept about half of STED resolution as a rule of oversampling.^{64–66} To reduce contributions from nanotube fluctuations, the line scans were aligned (Figure 2c, see also Section S4 in the Supporting Information). Subsequent averaging allowed identifying two clearly resolved fluorescence maxima arising from the two tube wall-crossing of the line scan; see Figure 2d. STED line scans that did not show two clear peaks after applying all of the

above-mentioned steps were discarded from the analysis; these discarded line scans represented approximately 56% of all scans collected and result from out-of-focus displacement, micropipette vibration, and membrane fluctuations. We denote the tube diameter determined from this interpeak distance as $2R_{t, \text{STED}}$ and measured it for different aspiration pressures ranging between $15\text{--}140 \times 10^{-6}$ N/m; see Figure S7 in the Supporting Information.

To avoid excessive photobleaching and decrease in fluorescence signal of the pulled nanotubes, each measurement at a given tension was performed only once. To estimate the precision of the image processing, we performed three repeat measurements on a single tube and found the standard deviation to be 11 nm.

We then aimed at comparing the tube diameter measured from the STED images, $2R_{t, \text{STED}}$, with the tube diameter, $2R_t$, indirectly assessed from the applied aspiration pressure following eq 3. For this, a precise knowledge of the membrane bending rigidity is required. The bending rigidity was measured with two independent methods. Analysis of the thermal fluctuations of free GUVs using a previously established protocol⁶² yielded for the bending rigidity $23 \pm 2 k_B T$ as assessed on five different vesicles (see Section S2 in the Supporting Information). We also measured this membrane elastic property from tube pulling experiments using eq 2 which gave a bending rigidity value of $23 \pm 5 k_B T$ as assessed from measurements on different vesicles (see Section S5 in the Supporting Information). The results from the two approaches are in excellent agreement and are consistent with previous data.⁶⁷

Using the obtained value for the bending rigidity ($\kappa = 23 k_B T$), we compared the diameters of tubes directly measured from the STED images, $2R_{t, \text{STED}}$, with the respective tube diameters, $2R_t$, independently assessed from the imposed membrane tension following eq 3. For the vesicles made of POPC/Chol we took $\kappa = 32.5 k_B T$ corresponding to the linearly proportional increase in the bending rigidity upon the incorporation of 10 mol % cholesterol in POPC membranes as reported in ref 68. The comparison shown in Figure 3 demonstrates that the experimental STED data and estimates from the elastic sheet model (with independently measured bending rigidity) are in excellent agreement. Presumably, for tube diameters approaching 50 nm and below, the accuracy of the STED measurements does not allow precise determination because the tube diameter reaches the size of a couple of pixels.

CONCLUSIONS

We have shown for the first time that super-resolution microscopy like STED can be used to directly measure the membrane nanotube diameter. For membrane tubes pulled in a controlled fashion from GUVs aspirated in micropipettes, the tube diameter measured microscopically is in excellent agreement with estimates inferred from knowledge of the membrane tension and membrane rigidity. Thus, we provide the first direct evidence for the validity of the widely used curvature elasticity model for nanotubes down to tube diameters of 50 nm. STED imaging of tubes pulled from vesicles of known bending rigidity offers a means of assessing the membrane tension without the need of operating micromanipulation setups such as micropipette aspiration.

In the current paper, we were able to measure the three quantities that enter eq 3 independently: the tube radius by STED, the aspiration tension Σ_{asp} from the aspiration pressure,

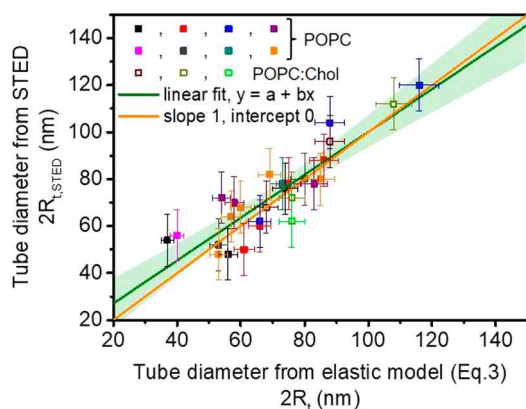


Figure 3. Plot of membrane nanotube diameters as directly measured using STED ($R_{i,STED}$) versus tube diameter estimated using eq 3 (R_i). Different colors correspond to measurements on different vesicles. Solid symbols represent data measured on POPC vesicles and open symbols are data collected on vesicles made of POPC/Chol 9:1 (molar ratio). The green line is a linear fit, $y = a + bx$, with $a = 8.86$ nm and $b = 0.91$, and the light green band represents a 95% confidence interval. The orange line with slope 1 is included for comparison.

and the bending rigidity by tube pulling. In this way, we were able to confirm eq 3 directly, see Figure 3. As it stands, eq 3 is based on the implicit assumption that the mechanical membrane tension is laterally uniform and that the mechanical tension Σ_t within the tube is equal to the aspiration tension. The latter assumption is, however, unnecessary. In fact, the mechanical balance within the nanotube leads to a slightly modified and more general form of eq 3 for which the aspiration tension is replaced by the tube tension Σ_t . As a consequence, the tube tension is given by $\Sigma_t = \kappa/(2R_t^2)$. The latter relation can be used to obtain the mechanical tube tension from the measured values of the bending rigidity and the tube radius. It will be interesting to use this more general form of eq 3 to estimate the tube tension of plasma membranes, combining the previously obtained bending rigidity of these membranes⁶⁹ with the tube radius as measured by STED.

Furthermore, assessing the tube tension from super-resolution imaging as introduced here could be applied, for example, to study (i) the dynamics of migratory cells leaving behind membrane nanotubes from which migratosomes with signaling material will be released,¹¹ (ii) curvature coupling of proteins to highly bent membranes,⁴⁶ as well as (iii) flows and tension propagation in cells⁴⁸ (it has already been shown that under the right conditions, STED microscopy can be applied to live-cell imaging without inducing substantial photo-damage⁷⁰) The analysis described here was limited to symmetric membranes with zero spontaneous curvature. Comparing the minimal forces needed to pull out tubes and the second term in eq 2 suggests that our approach can be extended to asymmetric membranes for which the magnitude of the spontaneous curvature is comparable to or larger than $1/(240$ nm). The imaging methodology developed here based on measuring tube diameters with STED offers access to direct measurements of material characteristics such as tension and rigidity of cell membranes.

■ ASSOCIATED CONTENT

Supporting Information

The Supporting Information is available free of charge at <https://pubs.acs.org/doi/10.1021/acs.nanolett.9b05232>.

Vesicles preparation and observation; fluctuation spectroscopy; setup; optical trapping and calibration; micropipette manipulation; STED imaging and image analysis; bending rigidity data from tube pulling (PDF) Fluctuating floppy vesicle suitable for micropipette aspiration (real time, 10 s at 24 frames per second) (AVI)

■ AUTHOR INFORMATION

Corresponding Author

Rumiana Dimova – Department of Theory and Bio-Systems, Max Planck Institute of Colloids and Interfaces, 14424 Potsdam, Germany; orcid.org/0000-0002-3872-8502; Email: dimova@mpikg.mpg.de

Authors

Debjit Roy – Department of Theory and Bio-Systems, Max Planck Institute of Colloids and Interfaces, 14424 Potsdam, Germany

Jan Steinkühler – Department of Theory and Bio-Systems, Max Planck Institute of Colloids and Interfaces, 14424 Potsdam, Germany; orcid.org/0000-0003-4226-7945

Ziliang Zhao – Department of Theory and Bio-Systems, Max Planck Institute of Colloids and Interfaces, 14424 Potsdam, Germany

Reinhard Lipowsky – Department of Theory and Bio-Systems, Max Planck Institute of Colloids and Interfaces, 14424 Potsdam, Germany; orcid.org/0000-0001-8417-8567

Complete contact information is available at: <https://pubs.acs.org/doi/10.1021/acs.nanolett.9b05232>

Author Contributions

R.D. and D.R. designed the experiments. D.R., J.S., and Z.Z. performed the experiments and analyzed the data. R.L. developed the theory. All authors wrote the manuscript.

Notes

The authors declare no competing financial interest.

■ ACKNOWLEDGMENTS

This work is part of the MaxSynBio consortium which is jointly funded by the Federal Ministry of Education and Research of Germany and the Max Planck Society. D.R. acknowledges helpful input from M. Karimi regarding micropipette manipulation.

■ REFERENCES

- (1) Diz-Munoz, A.; Krieg, M.; Bergert, M.; Ibarlucea-Benitez, I.; Muller, D. J.; Paluch, E.; Heisenberg, C. P. Control of Directed Cell Migration In Vivo by Membrane-to-Cortex Attachment. *PLoS Biol.* **2010**, *8* (11), e1000544.
- (2) Hanna, S. J.; McCoy-Simandle, K.; Miskolci, V.; Guo, P.; Cammer, M.; Hodgson, L.; Cox, D. The Role of Rho-GTPases and actin polymerization during Macrophage Tunneling Nanotube Biogenesis. *Sci. Rep.* **2017**, *7* (1), 8547–8547.
- (3) Chauveau, A.; Aucher, A.; Eissmann, P.; Vivier, E.; Davis, D. M. Membrane nanotubes facilitate long-distance interactions between natural killer cells and target cells. *Proc. Natl. Acad. Sci. U. S. A.* **2010**, *107* (12), 5545.

- (4) Kumar, A.; Kim, J. H.; Ranjan, P.; Metcalfe, M. G.; Cao, W.; Mishina, M.; Gangappa, S.; Guo, Z.; Boyden, E. S.; Zaki, S.; York, L.; García-Sastre, A.; Shaw, M.; Sambhara, S. Influenza virus exploits tunneling nanotubes for cell-to-cell spread. *Sci. Rep.* **2017**, *7*, 40360.
- (5) Lou, E.; Fujisawa, S.; Morozov, A.; Barlas, A.; Romin, Y.; Dogan, Y.; Gholami, S.; Moreira, A. L.; Manova-Todorova, K.; Moore, M. A. S. Tunneling Nanotubes Provide a Unique Conduit for Intercellular Transfer of Cellular Contents in Human Malignant Pleural Mesothelioma. *PLoS One* **2012**, *7* (3), e33093.
- (6) Rustom, A.; Saffrich, R.; Markovic, I.; Walther, P.; Gerdes, H. H. Nanotubular highways for intercellular organelle transport. *Science* **2004**, *303* (5660), 1007–1010.
- (7) Wang, Z.-G.; Liu, S.-L.; Tian, Z.-Q.; Zhang, Z.-L.; Tang, H.-W.; Pang, D.-W. Myosin-Driven Intercellular Transportation of Wheat Germ Agglutinin Mediated by Membrane Nanotubes between Human Lung Cancer Cells. *ACS Nano* **2012**, *6* (11), 10033–10041.
- (8) Haimovich, G.; Ecker, C. M.; Dunagin, M. C.; Eggan, E.; Raj, A.; Gerst, J. E.; Singer, R. H. Intercellular mRNA trafficking via membrane nanotube-like extensions in mammalian cells. *Proc. Natl. Acad. Sci. U. S. A.* **2017**, *114* (46), E9873–E9882.
- (9) Shen, J.; Zhang, J.-H.; Xiao, H.; Wu, J.-M.; He, K.-M.; Lv, Z.-Z.; Li, Z.-J.; Xu, M.; Zhang, Y.-Y. Mitochondria are transported along microtubules in membrane nanotubes to rescue distressed cardiomyocytes from apoptosis. *Cell Death Dis.* **2018**, *9* (2), 81.
- (10) Wang, X.; Gerdes, H.-H. Long-distance electrical coupling via tunneling nanotubes. *Biochim. Biophys. Acta, Biomembr.* **2012**, *1818* (8), 2082–2086.
- (11) Ma, L.; Li, Y.; Peng, J.; Wu, D.; Zhao, X.; Cui, Y.; Chen, L.; Yan, X.; Du, Y.; Yu, L. Discovery of the migrasome, an organelle mediating release of cytoplasmic contents during cell migration. *Cell Res.* **2015**, *25* (1), 24–38.
- (12) Lipowsky, R. Remodeling of membrane compartments: some consequences of membrane fluidity. *Biol. Chem.* **2014**, *395* (3), 253–74.
- (13) Lipowsky, R. Spontaneous tubulation of membranes and vesicles reveals membrane tension generated by spontaneous curvature. *Faraday Discuss.* **2013**, *161*, 305–331.
- (14) Sachs, F. Mechanical Transduction and the Dark Energy of Biology. *Biophys. J.* **2018**, *114* (1), 3–9.
- (15) Heinrich, V.; Waugh, R. E. A piconewton force transducer and its application to measurement of the bending stiffness of phospholipid membranes. *Ann. Biomed. Eng.* **1996**, *24* (5), 595–605.
- (16) Sorre, B.; Callan-Jones, A.; Manneville, J. B.; Nassoy, P.; Joanny, J. F.; Prost, J.; Goud, B.; Bassereau, P. Curvature-driven lipid sorting needs proximity to a demixing point and is aided by proteins. *Proc. Natl. Acad. Sci. U. S. A.* **2009**, *106* (14), 5622–5626.
- (17) Dasgupta, R.; Miettinen, M. S.; Fricke, N.; Lipowsky, R.; Dimova, R. The glycolipid GM1 reshapes asymmetric biomembranes and giant vesicles by curvature generation. *Proc. Natl. Acad. Sci. U. S. A.* **2018**, *115*, 5756–5761.
- (18) Waugh, R. E.; Evans, E. A. Thermoelasticity of red blood cell membrane. *Biophys. J.* **1979**, *26*, 115–132.
- (19) Hochmuth, R. M.; Mohandas, N.; Blackshear, P. L. Measurement of Elastic-Modulus for Red-Cell Membrane Using a Fluid Mechanical Technique. *Biophys. J.* **1973**, *13* (8), 747–762.
- (20) Colom, A.; Derivery, E.; Soleimanpour, S.; Tomba, C.; Molin, M. D.; Sakai, N.; González-Gaitán, M.; Matile, S.; Roux, A. A fluorescent membrane tension probe. *Nat. Chem.* **2018**, *10* (11), 1118–1125.
- (21) Aimon, S.; Callan-Jones, A.; Berthaud, A.; Pinot, M.; Toombes, G. E. S.; Bassereau, P. Membrane Shape Modulates Transmembrane Protein Distribution. *Dev. Dev. Cell* **2014**, *28* (2), 212–218.
- (22) Simunovic, M.; Evergren, E.; Golushko, I.; Prévost, C.; Renard, H.-F.; Johannes, L.; McMahan, H. T.; Lorman, V.; Voth, G. A.; Bassereau, P. How curvature-generating proteins build scaffolds on membrane nanotubes. *Proc. Natl. Acad. Sci. U. S. A.* **2016**, *113* (40), 11226.
- (23) Ramakrishnan, N.; Sreeja, K. K.; Roychoudhury, A.; Eckmann, D. M.; Ayyaswamy, P. S.; Baumgart, T.; Pucadyil, T.; Patil, S.; Weaver, V. M.; Radhakrishnan, R. Excess area dependent scaling behavior of nano-sized membrane tethers. *Phys. Biol.* **2018**, *15* (2), No. 026002.
- (24) Stepanyants, N.; Jeffries, G. D. M.; Orwar, O.; Jesorka, A. Radial Sizing of Lipid Nanotubes Using Membrane Displacement Analysis. *Nano Lett.* **2012**, *12* (3), 1372–1378.
- (25) Barooji, Y. F.; Rørvig-Lund, A.; Semsey, S.; Reihani, S. N. S.; Bendix, P. M. Dynamics of membrane nanotubes coated with I-BAR. *Sci. Rep.* **2016**, *6*, 30054.
- (26) Stachowiak, J. C.; Schmid, E. M.; Ryan, C. J.; Ann, H. S.; Sasaki, D. Y.; Sherman, M. B.; Geissler, P. L.; Fletcher, D. A.; Hayden, C. C. Membrane bending by protein-protein crowding. *Nat. Cell Biol.* **2012**, *14* (9), 944–949.
- (27) Pontes, B.; Monzo, P.; Gauthier, N. C. Membrane tension: A challenging but universal physical parameter in cell biology. *Semin. Cell Dev. Biol.* **2017**, *71*, 30–41.
- (28) Dimova, R.; Marques, C. *The Giant Vesicle Book*; Taylor & Francis Group, LLC: Boca Raton, 2019.
- (29) Dimova, R. Giant Vesicles and Their Use in Assays for Assessing Membrane Phase State, Curvature, Mechanics, and Electrical Properties. *Annu. Rev. Biophys.* **2019**, *48* (1), 93–119.
- (30) Dimova, R.; Aranda, S.; Bezlyepkina, N.; Nikolov, V.; Riske, K. A.; Lipowsky, R. A practical guide to giant vesicles. Probing the membrane nanoregime via optical microscopy. *J. Phys.: Condens. Matter* **2006**, *18* (28), S1151–S1176.
- (31) Rossier, O.; Cuvelier, D.; Borghi, N.; Puech, P. H.; Derenyi, I.; Buguin, A.; Nassoy, P.; Brochard-Wyart, F. Giant vesicles under flows: Extrusion and retraction of tubes. *Langmuir* **2003**, *19* (3), 575–584.
- (32) Borghi, N.; Rossier, O.; Brochard-Wyart, F. Hydrodynamic extrusion of tubes from giant vesicles. *EPL (Europhysics Letters)* **2003**, *64* (6), 837.
- (33) Huang, Z. H.; Abkarian, M.; Viallat, A. Sedimentation of vesicles: from pear-like shapes to microtether extrusion. *New J. Phys.* **2011**, *13*, No. 035026.
- (34) Dasgupta, R.; Dimova, R. Inward and outward membrane tubes pulled from giant vesicles. *J. Phys. D: Appl. Phys.* **2014**, *47* (28), 282001.
- (35) Bo, L.; Waugh, R. E. Determination of Bilayer-Membrane Bending Stiffness by Tether Formation from Giant, Thin-Walled Vesicles. *Biophys. J.* **1989**, *55* (3), 509–517.
- (36) Cans, A. S.; Wittenberg, N.; Karlsson, R.; Sombers, L.; Karlsson, M.; Orwar, O.; Ewing, A. Artificial cells: Unique insights into exocytosis using liposomes and lipid nanotubes. *Proc. Natl. Acad. Sci. U. S. A.* **2003**, *100* (2), 400–404.
- (37) Shnyrova, A. V.; Bashkurov, P. V.; Akimov, S. A.; Pucadyil, T. J.; Zimmerberg, J.; Schmid, S. L.; Frolov, V. A. Geometric Catalysis of Membrane Fission Driven by Flexible Dynamin Rings. *Science* **2013**, *339* (6126), 1433–1436.
- (38) Koster, G.; Cacciuto, A.; Derényi, I.; Frenkel, D.; Dogterom, M. Force Barriers for Membrane Tube Formation. *Phys. Rev. Lett.* **2005**, *94* (6), No. 068101.
- (39) Cuvelier, D.; Derenyi, I.; Bassereau, P.; Nassoy, P. Coalescence of membrane tethers: experiments, theory, and applications. *Biophys. J.* **2005**, *88* (4), 2714–2726.
- (40) Prévost, C.; Tsai, F.-C.; Bassereau, P.; Simunovic, M. Pulling Membrane Nanotubes from Giant Unilamellar Vesicles. *J. Visualized Exp.* **2017**, *130*, No. e56086.
- (41) Lipowsky, R. Understanding Membranes and Vesicles: A Personal Recollection of the Last Two Decades. In *Physics of Biological Membranes*; Bassereau, P., Sens, P., Eds.; Springer International Publishing: Cham, 2018; pp 3–44.
- (42) Tinevez, J.-Y.; Schulze, U.; Salbreux, G.; Roensch, J.; Joanny, J.-F.; Paluch, E. Role of cortical tension in bleb growth. *Proc. Natl. Acad. Sci. U. S. A.* **2009**, *106* (44), 18581.
- (43) Evans, E. A.; Waugh, R.; Melnik, L. Elastic area compressibility modulus of red cell membrane. *Biophys. J.* **1976**, *16* (6), 585–595.
- (44) Waugh, R.; Hochmuth, R. Mechanical equilibrium of thick, hollow, liquid membrane cylinders. *Biophys. J.* **1987**, *52*, 391–400.

- (45) Lamour, G.; Allard, A.; Pelta, J.; Labdi, S.; Lenz, M.; Campillo, C. Mapping and Modeling the Nanomechanics of Bare and Protein-Coated Lipid Nanotubes. *Phys. Rev. X* **2020**, *10* (1), No. 011031.
- (46) Sorre, B.; Callan-Jones, A.; Manzi, J.; Goud, B.; Prost, J.; Bassereau, P.; Roux, A. Nature of curvature coupling of amphiphysin with membranes depends on its bound density. *Proc. Natl. Acad. Sci. U. S. A.* **2012**, *109* (1), 173–178.
- (47) Bhatia, T. An image-processing method to detect sub-optical features based on understanding noise in intensity measurements. *Eur. Biophys. J.* **2018**, *47* (5), 531–538.
- (48) Shi, Z.; Graber, Z. T.; Baumgart, T.; Stone, H. A.; Cohen, A. E. Cell Membranes Resist Flow. *Cell* **2018**, *175* (7), 1769–1779.
- (49) Tian, A.; Baumgart, T. Sorting of Lipids and Proteins in Membrane Curvature Gradients. *Biophys. J.* **2009**, *96* (7), 2676–2688.
- (50) Liu, Y.; Agudo-Canalejo, J.; Grafmüller, A.; Dimova, R.; Lipowsky, R. Patterns of Flexible Nanotubes Formed by Liquid-Ordered and Liquid-Disordered Membranes. *ACS Nano* **2016**, *10* (1), 463–474.
- (51) Karimi, M.; Steinkühler, J.; Roy, D.; Dasgupta, R.; Lipowsky, R.; Dimova, R. Asymmetric Ionic Conditions Generate Large Membrane Curvatures. *Nano Lett.* **2018**, *18* (12), 7816–7821.
- (52) Bassereau, P.; Jin, R.; Baumgart, T.; Deserno, M.; Dimova, R.; Frolov, V. A.; Bashkurov, P. V.; Grubmüller, H.; Jahn, R.; Risselada, H. J.; Johannes, L.; Kozlov, M. M.; Lipowsky, R.; Pucadyil, T. J.; Zeno, W. F.; Stachowiak, J. C.; Stamou, D.; Breuer, A.; Lauritsen, L.; Simon, C.; Sykes, C.; Voth, G. A.; Weikl, T. R. The 2018 biomembrane curvature and remodeling roadmap. *J. Phys. D: Appl. Phys.* **2018**, *51* (34), 343001.
- (53) Sahl, S. J.; Hell, S. W.; Jakobs, S. Fluorescence nanoscopy in cell biology. *Nat. Rev. Mol. Cell Biol.* **2017**, *18*, 685.
- (54) Hell, S. W.; Sahl, S. J.; Bates, M.; Zhuang, X.; Heintzmann, R.; Booth, M. J.; Bewersdorf, J.; Shtengel, G.; Hess, H.; Tinnefeld, P.; Honigmann, A.; Jakobs, S.; Testa, I.; Cognet, L.; Lounis, B.; Ewers, H.; Davis, S. J.; Eggeling, C.; Klenerman, D.; Willig, K. I.; Vicidomini, G.; Castello, M.; Diaspro, A.; Cordes, T. The 2015 super-resolution microscopy roadmap. *J. Phys. D: Appl. Phys.* **2015**, *48* (44), 443001.
- (55) Honigmann, A.; Mueller, V.; Hell, S. W.; Eggeling, C. STED microscopy detects and quantifies liquid phase separation in lipid membranes using a new far-red emitting fluorescent phosphoglycerolipid analogue. *Faraday Discuss.* **2013**, *161* (0), 77–89.
- (56) Honigmann, A.; Mueller, V.; Ta, H.; Schoenle, A.; Sezgin, E.; Hell, S. W.; Eggeling, C. Scanning STED-FCS reveals spatiotemporal heterogeneity of lipid interaction in the plasma membrane of living cells. *Nat. Commun.* **2014**, *5*, 5412.
- (57) Sezgin, E.; Schneider, F.; Zilles, V.; Urbančič, I.; Garcia, E.; Waithé, D.; Klymchenko, A. S.; Eggeling, C. Polarity-Sensitive Probes for Superresolution Stimulated Emission Depletion Microscopy. *Biophys. J.* **2017**, *113* (6), 1321–1330.
- (58) Barentine, A. E. S.; Schroeder, L. K.; Graff, M.; Baddeley, D.; Bewersdorf, J. Simultaneously Measuring Image Features and Resolution in Live-Cell STED Images. *Biophys. J.* **2018**, *115* (6), 951–956.
- (59) Betzig, E.; Patterson, G. H.; Sougrat, R.; Lindwasser, O. W.; Olenych, S.; Bonifacino, J. S.; Davidson, M. W.; Lippincott-Schwartz, J.; Hess, H. F. Imaging Intracellular Fluorescent Proteins at Nanometer Resolution. *Science* **2006**, *313* (5793), 1642.
- (60) Huang, B.; Bates, M.; Zhuang, X. Super-resolution fluorescence microscopy. *Annu. Rev. Biochem.* **2009**, *78*, 993–1016.
- (61) Nienhaus, K.; Nienhaus, G. U. Where Do We Stand with Super-Resolution Optical Microscopy? *J. Mol. Biol.* **2016**, *428*, 308–322.
- (62) Gracià, R. S.; Bezlyepkina, N.; Knorr, R. L.; Lipowsky, R.; Dimova, R. Effect of cholesterol on the rigidity of saturated and unsaturated membranes: fluctuation and electrodeformation analysis of giant vesicles. *Soft Matter* **2010**, *6* (7), 1472–1482.
- (63) Kraikivski, P.; Pouligny, B.; Dimova, R. Implementing both short- and long-working-distance optical trappings into a commercial microscope. *Rev. Sci. Instrum.* **2006**, *77* (11), 113703.
- (64) Punge, A.; Rizzoli, S. O.; Jahn, R.; Wildanger, J. D.; Meyer, L.; Schönle, A.; Kastrop, L.; Hell, S. W. 3D reconstruction of high-resolution STED microscope images. *Microsc. Res. Tech.* **2008**, *71* (9), 644–650.
- (65) Lauterbach, M. A.; Keller, J.; Schönle, A.; Kamin, D.; Westphal, V.; Rizzoli, S. O.; Hell, S. W. Comparing video-rate STED nanoscopy and confocal microscopy of living neurons. *J. Biophotonics* **2010**, *3* (7), 417–424.
- (66) Wildanger, D.; Medda, R.; Kastrop, L.; Hell, S. W. A compact STED microscope providing 3D nanoscale resolution. *J. Microsc.* **2009**, *236* (1), 35–43.
- (67) Dimova, R. Recent developments in the field of bending rigidity measurements on membranes. *Adv. Colloid Interface Sci.* **2014**, *208* (0), 225–234.
- (68) Henriksen, J.; Rowat, A. C.; Brief, E.; Hsueh, Y. W.; Thewalt, J. L.; Zuckermann, M. J.; Ipsen, J. H. Universal behavior of membranes with sterols. *Biophys. J.* **2006**, *90* (5), 1639–1649.
- (69) Steinkühler, J.; Sezgin, E.; Urbančič, I.; Eggeling, C.; Dimova, R. Mechanical properties of plasma membrane vesicles correlate with lipid order, viscosity and cell density. *Communications Biology* **2019**, *2* (1), 337.
- (70) Kilian, N.; Goryaynov, A.; Lessard, M. D.; Hooker, G.; Toomre, D.; Rothman, J. E.; Bewersdorf, J. Assessing photodamage in live-cell STED microscopy. *Nat. Methods* **2018**, *15* (10), 755–756.

The mechanical tension of biomembranes can be measured by super resolution (STED) microscopy of force-induced nanotubes

Debjit Roy^{1,2}, Jan Steinkühler¹, Ziliang Zhao¹, Reinhard Lipowsky¹ and Rumiana Dimova^{1*}

¹Department of Theory and Bio-Systems, Max Planck Institute of Colloids and Interfaces, Science Park Golm, 14424 Potsdam, Germany

²Present address: Department of Biochemistry and Molecular Biophysics, Washington University School of Medicine, St. Louis, Missouri 63110, USA

* Address correspondence to Rumiana.Dimova@mpikg.mpg.de

S1 Vesicle preparation

Giant unilamellar vesicles (GUVs) were prepared using the electroformation method¹⁻². The vesicles were prepared from 1-palmitoyl-2-oleoyl-sn-glycero-3-phosphatidylcholine (POPC) (Avanti Polar Lipids) dissolved in chloroform at concentration of 2 mM. To ensure adhesion between GUVs and streptavidin coated beads, the membrane was doped with 0.1 mol% of biotinyl cap phosphatidylethanolamine (PE) (Avanti Polar Lipids). The membrane was stained with the fluorescent dye 0.5 mol% ATTO 647N (ATTO Tech). 4 μ l of the lipid solution was spread uniformly on the conductive sides of two indium tin oxide coated glass plates, and dried under vacuum for one hour to evaporate the chloroform. The two glass plates were assembled using a 2 mm thick Teflon spacer to form a closed chamber of volume \sim 1700 μ l. 100 mOsm/kg sucrose solution was used to fill the chamber as growing medium. The solution osmolarity as well as that of the external vesicle solution was adjusted with freezing point osmometer Osmomat 3000 (Gonotec). A sinusoidal AC electric field at 10 Hz frequency with RMS amplitude 0.75 V, measured at the ITO coated glass plates, was applied for the electrosweeling process for 2 hours. The grown GUVs were harvested afterwards and transferred to glass containers for further investigations. All experiments were performed at room temperature (\sim 22°C).

S2 Fluctuation analysis

The bending rigidity of a GUV can be obtained by analyzing the thermal fluctuations of the equatorial plane contour. Following a previously published protocol³, for each vesicle, 10000 snapshots were collected at an acquisition speed of 50 frames per second with 200 μ s exposure time using a fast digital camera HG-100K (Redlake Inc., USA). The vesicles were recorded at their focal on inverted microscope Axiovert 135. The measurements were done under the same buffer condition at which the tube pulling experiments were performed. From the shape fluctuation analysis of five GUVs, the average bending rigidity is found to be (23 ± 2) $k_B T$, see Table S1 for data on the individual measurements.

Table S1. Bending rigidity obtained from fluctuation analysis. The numbers in the brackets indicate the measurement error.

GUV Number	Bending Rigidity, $k_B T$
1	23 (2)
2	25 (3)
3	21 (3)
4	22 (2)
5	25 (2)
Average Value	23 ± 2

S3 Experimental setup

The experimental set-up consists of three parts: micropipette system to hold and aspirate GUVs, optical tweezers to extract membrane nanotube and confocal and STED scanning for the fluorescence imaging as shown in Fig. 1 in the main text. The setup allowed us to measure the nanotube diameter at varying aspiration pressures using STED microscopy. The schematic of all the optical components of the set-up is shown in Fig. S1.

S3.1 Optical tweezers setup and calibration

The optical tweezers was built on a STED imaging system (Abberior GmbH, Germany) based on Olympus IX83 (Olympus Inc.) microscope. An expanded and collimated TEM₀₀ mode continuous wave laser beam centered at 1064 nm wavelength from a Nd:YAG laser (YLR-10-LP, IPG Photonics Corp.) was inserted from the back port of the microscope to the sample stage through a 60× water immersion objective (NA 1.2, UPLSAPO60, Olympus Inc., Japan) to form a stable optical trap. The typical laser power used for trapping was 100 mW at the sample. The bright field image of the trapped object was collected using a monochromatic CCD camera (JENOPTIK "ProgRes M") positioned at the back port of the microscope.

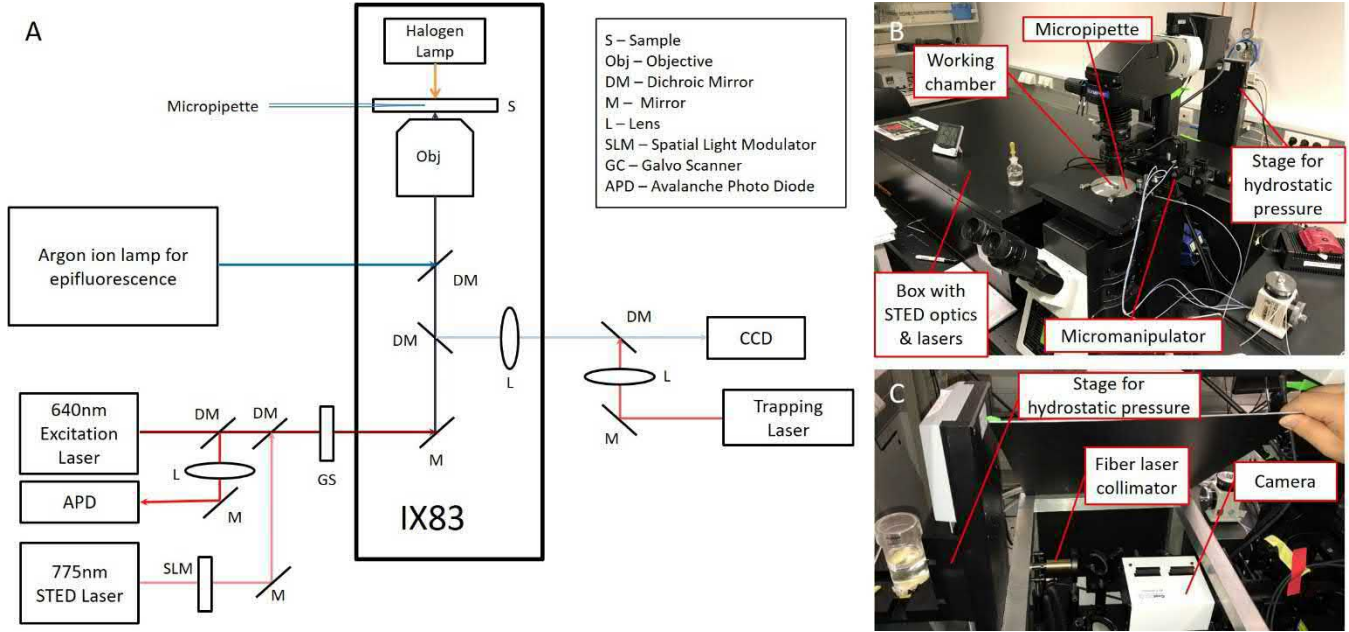


Figure S1. (A) Basic schematics of the main components of the experimental setup for STED imaging and optical trapping, and pictures of the front view (B) and the back view (C) of the actual setup with indicated components.

The trap stiffness (κ_{tr}) was calibrated using the viscous drag method, where the sample is displaced at different constant velocities (v) below the escape velocity while holding the bead with the tweezers. Using a motorized stage (BX3-SSU-1-2 motorized xy-table), the sample was displaced along the axis at which the nanotube is being pulled. The position of the trapped bead was determined using centroid tracking algorithm⁴ written in MATLAB (Mathworks Inc) where the particle position is estimated from frame-to-frame using a cross-correlation peak centroid estimation technique⁵. All measurements were performed at a height of $\sim 20 \mu\text{m}$ above the glass boundary of the sample chamber. The force on a bead with radius r exposed to drag from the surrounding medium with dynamic viscosity η is given by:

$$f_{dr} = 6\pi r\eta v \quad (S1)$$

The force F_{dr} changes the position of the trapped bead from its equilibrium position in the center of the trap, x_0 , to a newer position, x . The force on the bead due to this off-centering $\Delta x = x - x_0$ is $f_x = \kappa_{tr}\Delta x$ balances the viscous drag force. Equating f_x with f_{dr} yields the trap stiffness

$$\kappa_{tr} = 6\pi r\eta \frac{v}{\Delta x} \quad (S2)$$

which we assess from the dependence of the off-center displacement from the stage velocity, see Fig. S2. The trap stiffness was found to be $(74 \pm 2) \text{ pN}/\mu\text{m}$ at our working conditions ($r = 1 \mu\text{m}$, $\eta = 0.93 \text{ mPa}\cdot\text{s}$).

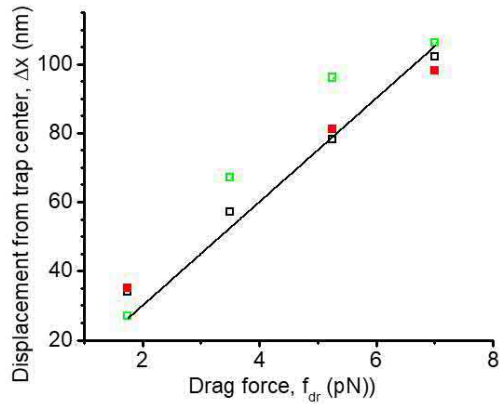


Figure S2. Plot of the viscous drag force, $f_{dr} = 6\pi\eta v$, vs. off-center displacement, Δx . Different colors correspond to different particles measured. The inverse slope of the linear fit yields the trap stiffness κ_{tr} .

The values of the trap stiffness can be used to estimate the typical fluctuation amplitude of the bead in the trap. The relation between the mean square displacement of the trapped bead (Δx^2) and κ_{tr} follows from the equipartition theorem:

$$\Delta x^2 = \frac{k_B T}{\kappa_{tr}} \quad (S3)$$

where, k_B is Boltzmann constant and T is experimental temperature. For $\kappa_{tr} = 74 \text{ pN}/\mu\text{m}$, the root mean square displacement ($\sqrt{\Delta x^2}$) is around $\sim 7.4 \text{ nm}$, inferring that the movement range of the trapped microsphere due to thermal motion is $\sim 15 \text{ nm}$ in x -axis.

S3.2 Working chamber and micropipette aspiration

Micropipettes were pulled from borosilicate capillaries (1B100-4, World Precision Instruments) using pipette puller (Sutter Instruments, Novato, CA). The tips of the prepared micropipettes were cut and shaped to desirable diameter ($3 \mu\text{m} - 5 \mu\text{m}$) using a microforge (Narishige Corp., Japan). Two coverslips of thickness $\sim 170 \mu\text{m}$ (No. 1.5) were fixed against each other separated by Π -shaped Teflon spacer to form a sample chamber of length $\sim 18 \text{ mm}$, width $\sim 15 \text{ mm}$ and height $\sim 2 \text{ mm}$. The cover glass chamber and the micropipette were coated with 1 mg/ml BSA solution to prevent the adhesion of the GUVs to them. Then they were rinsed using the external vesicle buffer (40 mM glucose and 30 mM NaCl). The sample chamber was mounted on the microscope stage. The vesicle solution diluted 20 times with isotonic experimental buffer was introduced in the sample chamber together with streptavidin-coated beads (Polyscience Inc., Cat #24160, with an average diameter of $\sim 1.9 \mu\text{m}$). The presence of NaCl salt was necessary for the strong non-covalent binding of biotin-streptavidin to pull the membrane nanotube⁶. With this combination of sugar and salt, the GUVs were able to form strong biotin-streptavidin bonds while their shapes were not deformed due to gravity. A micropipette was inserted from the open end of the sample chamber using a three dimensional water hydraulic micromanipulator system (Narishige Corp., Japan) clamped to the microscope. Zero pressure across the micropipette tip, positioned at $20 \mu\text{m}$ above the cover glass (the height of the tube-pulling experiment), was calibrated by watching the flow of streptavidin-coated particles near and inside the micropipette tip. To avoid evaporation, the water-air interface at the open side of the chamber was then covered by a drop of mineral oil. The micropipette aspiration of GUVs was controlled through a water reservoir placed on a vertical motorized linear translational stage (M-531.DD, Physik Instrumente, Germany) connected to the pipette holder. For extruding a membrane nanotube from the vesicle, a floppy GUV was held at a low aspiration pressure and brought into contact with an optically trapped streptavidin bead for few seconds. The floppiness and low aspiration tensions allow for the manipulated bead to be brought in contact with a larger fraction of the vesicle membrane (tense vesicles will allow only for point contact between the bead and vesicle) resulting in stronger adhesion as required for pulling out tubes. Then, by means of displacing the aspiration pipette mounted on a micromanipulator, the aspirated GUV was displaced away from the trapped bead by $\sim 10 \mu\text{m}$. Due to the strong biotin-streptavidin bonding, a thin membrane nanotube is formed in this process. Then the aspiration pressure was increased so that the length of the GUV tongue inside the micropipette is higher than the micropipette radius. The membrane nanotube diameter was measured by STED scanning of the extruded membrane nanotube at different aspiration pressures.

S3.3 3D STED imaging and comparison to 2D STED

To measure the diameter of the membrane nanotube, 3D STED line scan was used. The STED microscopic system (Abberior GmbH, Germany) is a commercial microscope based on an inverted microscope (IX83, Olympus Inc., Japan). The STED system contains four lasers at 405 nm, 480 nm, 561 nm and 640 nm for fluorescence excitation, allowing multicolor imaging (not employed in this work). The depletion laser is centered at 775 nm. In the path of the STED laser, a spatial light modulator (SLM) is present to generate both 2D and 3D STED beams, see Fig. S1. Both the fluorescence excitation and STED beams are focused onto the sample by the same objective which is used for the optical trapping after passing through a galvo-scanning mirror unit. Fluorescence signal generated from the sample is collected by the same objective and passed through a confocal pinhole to discard the out-of-focus signal and finally focused onto APD detectors (Fig. S1). In our experiments, the 640 nm laser was used for fluorescence excitation. As the imaging was performed 20 μm above the cover glass, a continuous auto-focus unit (ZDC2, Olympus Inc., Japan) was used. The beam profile of fluorescence excitation and 3D STED beam were measured using 150 nm gold nanoparticles (Abberior Nanoparticle Set for Expert Line 595 & 775 nm, Item number: AS-595-775-NP) as shown in Fig. S3.

The STED resolution was measured by 28 nm diameter crimson microspheres (F8782, Invitrogen) and found to be < 40 nm (Fig. S4). Thus, our STED system is capable of measuring diameter of the membrane nanotubes with radius larger than 40 nm. The 2D STED images are much brighter compared to those acquired with 3D STED at the same experimental condition, but the 2D STED images include fluorescence signal originating from out-of-focus parts of the membrane nanotube because of poor axial resolution⁷. This effectively leads to a decrease in the resolution preventing the clear detection of the two wall cross-sections of the nanotubes. This is demonstrated in Fig. S5, where the line profile across a membrane tube shows different peak heights – higher for the 2D STED image, but with resolvable peaks in 3D STED profile. The two peaks in the 3D STED line profile denote the two wall-crossings of the nanotube which cannot be detected in the 2D STED line scan where light is collected practically from the whole tube cross-section, the z-resolution being roughly 120 nm in this case. We explored pixel sizes of 5 nm, 10 nm and 20 nm when performing the line scanning and found that with decrease in the pixel size, the data contains more noise from nanotube fluctuation and has more peaks (Fig. S6). Note that scanning with smaller pixel size requires longer time lead to more vibration of the nanotube and hence noisier data. Thus, 20 nm pixel size was chosen for the experiments. Also, 20 nm pixel size is half of the STED resolution which is typical for STED scanning⁸.

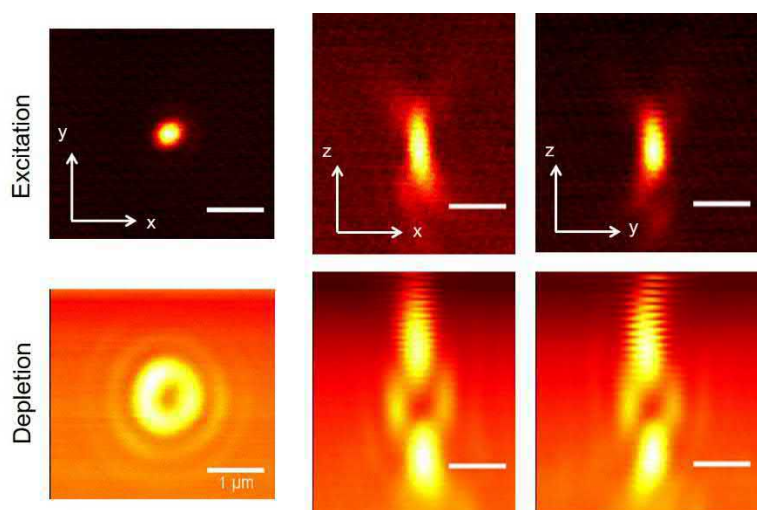


Figure S3: The beam profile of excitation laser (640 nm) (top) and 3D depletion laser (775 nm) (bottom) shown in the xy-plane (left), xz-plane (middle) and yz-plane (right). These profiles were measured using the reflection from 150 nm gold nanoparticles. Scale bars: 1 μm .

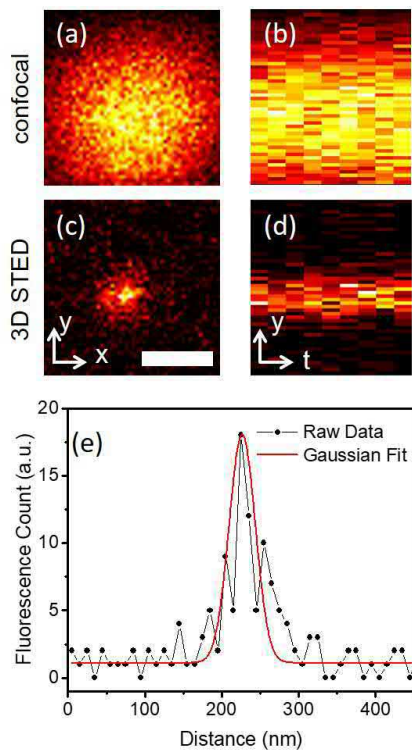


Figure S4: Confocal (a) and 3D STED (c) image of 28 nm crimson beads immobilized on a cover slip. The pixel size was set to 10 nm. The scale bar corresponds to 200 nm. Kymograph of the same crimson bead in y axis (perpendicular to membrane nanotube) for (b) confocal and (d) 3D STED scanning. Nine line scans were performed at 10 μ s pixel dwell time with 10 nm pixel size (each line scan takes 0.5 ms). (e): Gaussian fitting of the y-line scan gives 3D STED resolution to be better than 40 nm.

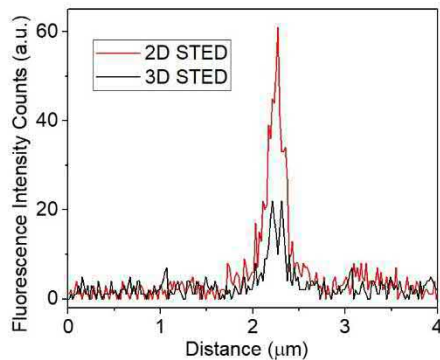


Figure S5. Intensity profile along a line scan across a membrane nanotube with 2D (red) and 3D (black) STED beams collected with pixel size of 20 nm. The 2D STED image is brighter but its effective resolution is lower due to the fluorescence signal arising from the out-of-focus part of the nanotube in z-axial direction. The signal-to-noise ratio for 3D STED is reduced but still sufficiently high (presumably because of the high quantum efficiency of the dye) to resolve the tube walls seen as peaks.

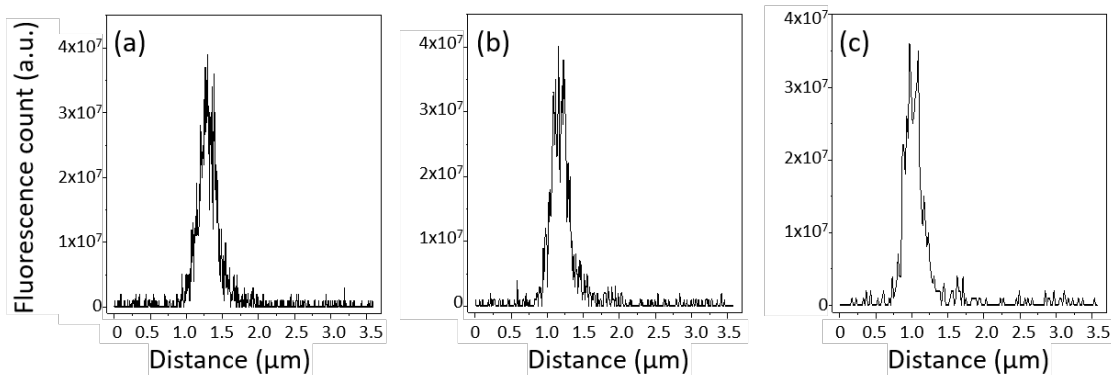


Figure S6. Line scan of a nanotube using (a) 5 nm, (b) 10 nm and (c) 20 nm pixel size. At 20 nm pixel size, the data not only becomes smoother (higher signal-to-noise ratio) but it also allows distinguishing the precise position of the two peaks indicative for the wall-crossings of the membrane nanotube.

S4 STED image analysis

To measure the tube diameter, a small image region (typically, $1 \times 1 \mu\text{m}$) including the extruded nanotube was chosen (typically in the middle of the nanotube) and 100 line scans were performed through the selected portion of the nanotube in direction perpendicular to its length (along the y-axis in Fig. 1b in the main text). The reliable and unbiased extraction of nanotube diameters was complicated by fluctuations of the nanotubes during the measurement. These fluctuations lead to a spatial displacement of the nanotube between individual scans (both in y- and z-directions, i.e. also out-of-focus), obscuring the extraction of the tube diameter. We employed an automated image analysis routine to align the individual line scans. An example of an experimentally obtained kymograph is shown in Fig. 2a in the main text. To obtain subpixel accuracy the individual line scans were linearly interpolated (interp1, MATLAB 2014a) to 0.1 pixel resolution. The individual line scans were then aligned by maximizing the overlap of the integrated intensity between two consecutive line scans l_j and l_j of length m as measured by

$$\max_{k \in \{-2m, 2m\}} \int l_{i+1}(n-k)l_i(n)dn$$

where the integral is evaluated numerically (trapz, MATLAB 2014a). The line scan l_i is shifted by the value of k at maximal overlap relative to the next lines scan with $i=i+1$. By iterating over all line scans, an aligned kymograph is obtained. As judged from the confocal image, the nanotube stays on average in focus during the measurement. The aligned line scans in the kymograph were then averaged as shown in Fig. 2d in the main text and the tube diameter determined from the distance between the two major maxima corresponding to the wall-crossing of the tube. Figure S7 shows the dependence of the measured tube diameter on the applied membrane tension of the aspirated vesicle (same data as in Fig. 3 in the main text).

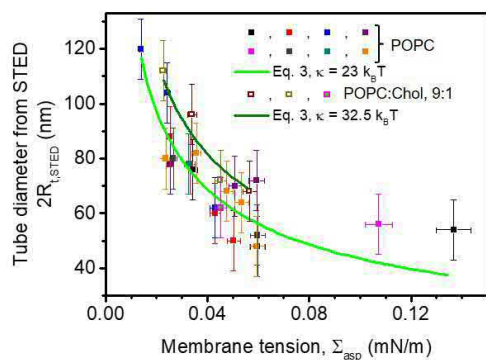


Figure S7. Plot of membrane nanotube diameter as directly measured using STED ($R_{t,STED}$) at varying membrane tension Σ_{asp} and for vesicles with two compositions – POPC (solid symbols) and POPC:Chol 9:1 (open symbols). Different colors correspond to measurements on different vesicles. The two curves show the calculated tube diameter using Eq. 3 in the main text with bending rigidity $\kappa = 23 k_B T$ as measured independently for POPC membranes, and $\kappa = 32.5 k_B T$ as assessed from literature values for membranes made of POPC:Chol 9:1.

S5 Tube pulling experiment for deducing the membrane bending rigidity

Pulling of outward membrane nanotubes from GUVs can be used to assess the membrane bending rigidity. For symmetric membranes, the pulling force is $f_t = 2\pi\sqrt{2\kappa\Sigma_{\text{asp}}} - 4\pi\kappa m - \pi\kappa/R_v$ (see main text for notations). Thus, the bending rigidity κ can be directly obtained from the slope of the dependence of the pulling force, f_t , vs. $\sqrt{\Sigma_{\text{asp}}}$ (Fig. S8). For this experiment, the trap force was measured from the displacement of the bead away from the trap center, Δx . Bright field images of the trapped bead were collected using the CCD camera at the back port of the microscope. The bead was first recorded free and then attached via a nanotube to the GUV held by a micropipette at different aspiration pressures. For each of these measurements, 100 frames were collected with 1 ms exposure time at 9 frames per second. As explained in Section S3.1, the sub-pixels bead position was determined using centroid tracking algorithm⁴. The trap force was then determined from $f_t = \kappa_{\text{tr}} \Delta x$ using the predetermined trap constant κ_{tr} .

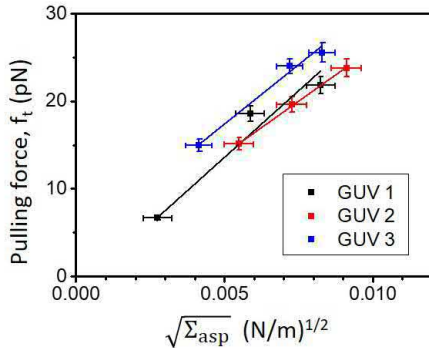


Figure S8. Pulling force versus the square root of membrane tension (Σ_{asp}) for three different GUVs. The solid lines are the linear fit for the data of the respective GUVs. The bending rigidity is found to be $\kappa = 23 \pm 5 \text{ k}_B T$.

Movie S1. Example for a fluctuating floppy vesicle suitable for micropipette aspiration (real time, 10 s at 24 frames per second). The scale bar corresponds to $10 \mu\text{m}$.

References

1. Angelova, M. I.; Dimitrov, D. S., Liposome Electroformation. *Faraday Discussions* **1986**, *81*, 303-311.
2. Dimova, R., Giant Vesicles and Their Use in Assays for Assessing Membrane Phase State, Curvature, Mechanics, and Electrical Properties. *Annu. Rev. Biophys.* **2019**, *48* (1), 93-119.
3. Gracià, R. S.; Bezlyepkina, N.; Knorr, R. L.; Lipowsky, R.; Dimova, R., Effect of cholesterol on the rigidity of saturated and unsaturated membranes: fluctuation and electrodeformation analysis of giant vesicles. *Soft Matter* **2010**, *6* (7), 1472-1482.
4. Dasgupta, R.; Verma, R. S.; Gupta, P. K., Microfluidic sorting with blinking optical traps. *Opt. Lett.* **2012**, *37* (10), 1739-1741.
5. Gelles, J.; Schnapp, B. J.; Sheetz, M. P., Tracking kinesin-driven movements with nanometre-scale precision. *Nature* **1988**, *331* (6155), 450-453.
6. Prévost, C.; Tsai, F.-C.; Bassereau, P.; Simunovic, M., Pulling Membrane Nanotubes from Giant Unilamellar Vesicles. *JoVE* **2017**, (130), e56086.
7. Sahl, S. J.; Hell, S. W.; Jakobs, S., Fluorescence nanoscopy in cell biology. *Nat. Rev. Mol. Cell Biol.* **2017**, *18*, 685.
8. Lauterbach, M. A.; Keller, J.; Schönle, A.; Kamin, D.; Westphal, V.; Rizzoli, S. O.; Hell, S. W., Comparing video-rate STED nanoscopy and confocal microscopy of living neurons. *Journal of Biophotonics* **2010**, *3* (7), 417-424.

The mechanical tension of biomembranes can be measured by super resolution (STED) microscopy of force-induced nanotubes

Debjit Roy^{1,2}, Jan Steinkühler¹, Ziliang Zhao¹, Reinhard Lipowsky¹ and Rumiana Dimova^{1*}

¹Department of Theory and Bio-Systems, Max Planck Institute of Colloids and Interfaces, Science Park Golm, 14424 Potsdam, Germany

²Present address: Department of Biochemistry and Molecular Biophysics, Washington University School of Medicine, St. Louis, Missouri 63110, USA

* Address correspondence to Rumiana.Dimova@mpikg.mpg.de

S1 Vesicle preparation

Giant unilamellar vesicles (GUVs) were prepared using the electroformation method¹⁻². The vesicles were prepared from 1-palmitoyl-2-oleoyl-sn-glycero-3-phosphatidylcholine (POPC) (Avanti Polar Lipids) dissolved in chloroform at concentration of 2 mM. To ensure adhesion between GUVs and streptavidin coated beads, the membrane was doped with 0.1 mol% of biotinyl cap phosphatidylethanolamine (PE) (Avanti Polar Lipids). The membrane was stained with the fluorescent dye 0.5 mol% ATTO 647N (ATTO Tech). 4 μ l of the lipid solution was spread uniformly on the conductive sides of two indium tin oxide coated glass plates, and dried under vacuum for one hour to evaporate the chloroform. The two glass plates were assembled using a 2 mm thick Teflon spacer to form a closed chamber of volume \sim 1700 μ l. 100 mOsm/kg sucrose solution was used to fill the chamber as growing medium. The solution osmolarity as well as that of the external vesicle solution was adjusted with freezing point osmometer Osmomat 3000 (Gonotec). A sinusoidal AC electric field at 10 Hz frequency with RMS amplitude 0.75 V, measured at the ITO coated glass plates, was applied for the electrosweeling process for 2 hours. The grown GUVs were harvested afterwards and transferred to glass containers for further investigations. All experiments were performed at room temperature (\sim 22°C).

S2 Fluctuation analysis

The bending rigidity of a GUV can be obtained by analyzing the thermal fluctuations of the equatorial plane contour. Following a previously published protocol³, for each vesicle, 10000 snapshots were collected at an acquisition speed of 50 frames per second with 200 μ s exposure time using a fast digital camera HG-100K (Redlake Inc., USA). The vesicles were recorded at their focal on inverted microscope Axiovert 135. The measurements were done under the same buffer condition at which the tube pulling experiments were performed. From the shape fluctuation analysis of five GUVs, the average bending rigidity is found to be (23 ± 2) $k_B T$, see Table S1 for data on the individual measurements.

Table S1. Bending rigidity obtained from fluctuation analysis. The numbers in the brackets indicate the measurement error.

GUV Number	Bending Rigidity, $k_B T$
1	23 (2)
2	25 (3)
3	21 (3)
4	22 (2)
5	25 (2)
Average Value	23 ± 2

S3 Experimental setup

The experimental set-up consists of three parts: micropipette system to hold and aspirate GUVs, optical tweezers to extract membrane nanotube and confocal and STED scanning for the fluorescence imaging as shown in Fig. 1 in the main text. The setup allowed us to measure the nanotube diameter at varying aspiration pressures using STED microscopy. The schematic of all the optical components of the set-up is shown in Fig. S1.

S3.1 Optical tweezers setup and calibration

The optical tweezers was built on a STED imaging system (Abberior GmbH, Germany) based on Olympus IX83 (Olympus Inc.) microscope. An expanded and collimated TEM₀₀ mode continuous wave laser beam centered at 1064 nm wavelength from a Nd:YAG laser (YLR-10-LP, IPG Photonics Corp.) was inserted from the back port of the microscope to the sample stage through a 60× water immersion objective (NA 1.2, UPLSAPO60, Olympus Inc., Japan) to form a stable optical trap. The typical laser power used for trapping was 100 mW at the sample. The bright field image of the trapped object was collected using a monochromatic CCD camera (JENOPTIK "ProgRes M") positioned at the back port of the microscope.

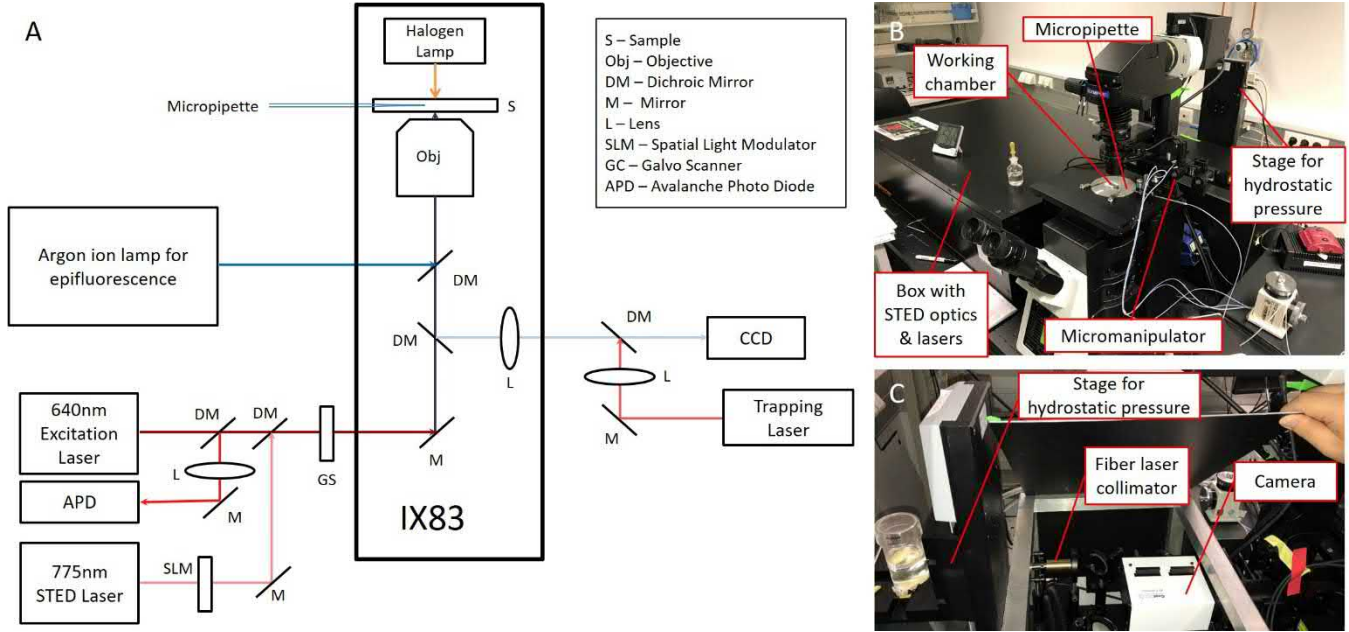


Figure S1. (A) Basic schematics of the main components of the experimental setup for STED imaging and optical trapping, and pictures of the front view (B) and the back view (C) of the actual setup with indicated components.

The trap stiffness (κ_{tr}) was calibrated using the viscous drag method, where the sample is displaced at different constant velocities (v) below the escape velocity while holding the bead with the tweezers. Using a motorized stage (BX3-SSU-1-2 motorized xy-table), the sample was displaced along the axis at which the nanotube is being pulled. The position of the trapped bead was determined using centroid tracking algorithm⁴ written in MATLAB (Mathworks Inc) where the particle position is estimated from frame-to-frame using a cross-correlation peak centroid estimation technique⁵. All measurements were performed at a height of $\sim 20 \mu\text{m}$ above the glass boundary of the sample chamber. The force on a bead with radius r exposed to drag from the surrounding medium with dynamic viscosity η is given by:

$$f_{dr} = 6\pi r\eta v \quad (S1)$$

The force F_{dr} changes the position of the trapped bead from its equilibrium position in the center of the trap, x_0 , to a newer position, x . The force on the bead due to this off-centering $\Delta x = x - x_0$ is $f_x = \kappa_{tr}\Delta x$ balances the viscous drag force. Equating f_x with f_{dr} yields the trap stiffness

$$\kappa_{tr} = 6\pi r\eta \frac{v}{\Delta x} \quad (S2)$$

which we assess from the dependence of the off-center displacement from the stage velocity, see Fig. S2. The trap stiffness was found to be $(74 \pm 2) \text{ pN}/\mu\text{m}$ at our working conditions ($r = 1 \mu\text{m}$, $\eta = 0.93 \text{ mPa}\cdot\text{s}$).

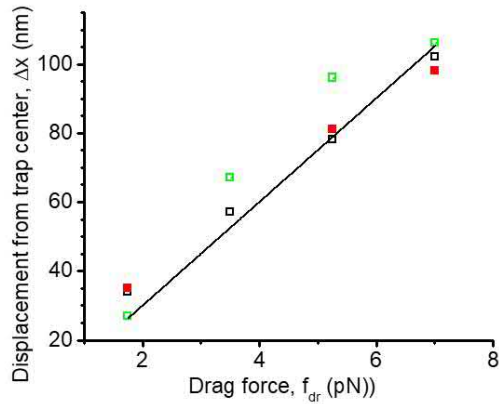


Figure S2. Plot of the viscous drag force, $f_{dr} = 6\pi\eta v$, vs. off-center displacement, Δx . Different colors correspond to different particles measured. The inverse slope of the linear fit yields the trap stiffness κ_{tr} .

The values of the trap stiffness can be used to estimate the typical fluctuation amplitude of the bead in the trap. The relation between the mean square displacement of the trapped bead (Δx^2) and κ_{tr} follows from the equipartition theorem:

$$\Delta x^2 = \frac{k_B T}{\kappa_{tr}} \quad (S3)$$

where, k_B is Boltzmann constant and T is experimental temperature. For $\kappa_{tr} = 74 \text{ pN}/\mu\text{m}$, the root mean square displacement ($\sqrt{\Delta x^2}$) is around $\sim 7.4 \text{ nm}$, inferring that the movement range of the trapped microsphere due to thermal motion is $\sim 15 \text{ nm}$ in x -axis.

S3.2 Working chamber and micropipette aspiration

Micropipettes were pulled from borosilicate capillaries (1B100-4, World Precision Instruments) using pipette puller (Sutter Instruments, Novato, CA). The tips of the prepared micropipettes were cut and shaped to desirable diameter ($3 \mu\text{m} - 5 \mu\text{m}$) using a microforge (Narishige Corp., Japan). Two coverslips of thickness $\sim 170 \mu\text{m}$ (No. 1.5) were fixed against each other separated by Π -shaped Teflon spacer to form a sample chamber of length $\sim 18 \text{ mm}$, width $\sim 15 \text{ mm}$ and height $\sim 2 \text{ mm}$. The cover glass chamber and the micropipette were coated with 1 mg/ml BSA solution to prevent the adhesion of the GUVs to them. Then they were rinsed using the external vesicle buffer (40 mM glucose and 30 mM NaCl). The sample chamber was mounted on the microscope stage. The vesicle solution diluted 20 times with isotonic experimental buffer was introduced in the sample chamber together with streptavidin-coated beads (Polyscience Inc., Cat #24160, with an average diameter of $\sim 1.9 \mu\text{m}$). The presence of NaCl salt was necessary for the strong non-covalent binding of biotin-streptavidin to pull the membrane nanotube⁶. With this combination of sugar and salt, the GUVs were able to form strong biotin-streptavidin bonds while their shapes were not deformed due to gravity. A micropipette was inserted from the open end of the sample chamber using a three dimensional water hydraulic micromanipulator system (Narishige Corp., Japan) clamped to the microscope. Zero pressure across the micropipette tip, positioned at $20 \mu\text{m}$ above the cover glass (the height of the tube-pulling experiment), was calibrated by watching the flow of streptavidin-coated particles near and inside the micropipette tip. To avoid evaporation, the water-air interface at the open side of the chamber was then covered by a drop of mineral oil. The micropipette aspiration of GUVs was controlled through a water reservoir placed on a vertical motorized linear translational stage (M-531.DD, Physik Instrumente, Germany) connected to the pipette holder. For extruding a membrane nanotube from the vesicle, a floppy GUV was held at a low aspiration pressure and brought into contact with an optically trapped streptavidin bead for few seconds. The floppiness and low aspiration tensions allow for the manipulated bead to be brought in contact with a larger fraction of the vesicle membrane (tense vesicles will allow only for point contact between the bead and vesicle) resulting in stronger adhesion as required for pulling out tubes. Then, by means of displacing the aspiration pipette mounted on a micromanipulator, the aspirated GUV was displaced away from the trapped bead by $\sim 10 \mu\text{m}$. Due to the strong biotin-streptavidin bonding, a thin membrane nanotube is formed in this process. Then the aspiration pressure was increased so that the length of the GUV tongue inside the micropipette is higher than the micropipette radius. The membrane nanotube diameter was measured by STED scanning of the extruded membrane nanotube at different aspiration pressures.

S3.3 3D STED imaging and comparison to 2D STED

To measure the diameter of the membrane nanotube, 3D STED line scan was used. The STED microscopic system (Abberior GmbH, Germany) is a commercial microscope based on an inverted microscope (IX83, Olympus Inc., Japan). The STED system contains four lasers at 405 nm, 480 nm, 561 nm and 640 nm for fluorescence excitation, allowing multicolor imaging (not employed in this work). The depletion laser is centered at 775 nm. In the path of the STED laser, a spatial light modulator (SLM) is present to generate both 2D and 3D STED beams, see Fig. S1. Both the fluorescence excitation and STED beams are focused onto the sample by the same objective which is used for the optical trapping after passing through a galvo-scanning mirror unit. Fluorescence signal generated from the sample is collected by the same objective and passed through a confocal pinhole to discard the out-of-focus signal and finally focused onto APD detectors (Fig. S1). In our experiments, the 640 nm laser was used for fluorescence excitation. As the imaging was performed 20 μm above the cover glass, a continuous auto-focus unit (ZDC2, Olympus Inc., Japan) was used. The beam profile of fluorescence excitation and 3D STED beam were measured using 150 nm gold nanoparticles (Abberior Nanoparticle Set for Expert Line 595 & 775 nm, Item number: AS-595-775-NP) as shown in Fig. S3.

The STED resolution was measured by 28 nm diameter crimson microspheres (F8782, Invitrogen) and found to be < 40 nm (Fig. S4). Thus, our STED system is capable of measuring diameter of the membrane nanotubes with radius larger than 40 nm. The 2D STED images are much brighter compared to those acquired with 3D STED at the same experimental condition, but the 2D STED images include fluorescence signal originating from out-of-focus parts of the membrane nanotube because of poor axial resolution⁷. This effectively leads to a decrease in the resolution preventing the clear detection of the two wall cross-sections of the nanotubes. This is demonstrated in Fig. S5, where the line profile across a membrane tube shows different peak heights – higher for the 2D STED image, but with resolvable peaks in 3D STED profile. The two peaks in the 3D STED line profile denote the two wall-crossings of the nanotube which cannot be detected in the 2D STED line scan where light is collected practically from the whole tube cross-section, the z-resolution being roughly 120 nm in this case. We explored pixel sizes of 5 nm, 10 nm and 20 nm when performing the line scanning and found that with decrease in the pixel size, the data contains more noise from nanotube fluctuation and has more peaks (Fig. S6). Note that scanning with smaller pixel size requires longer time lead to more vibration of the nanotube and hence noisier data. Thus, 20 nm pixel size was chosen for the experiments. Also, 20 nm pixel size is half of the STED resolution which is typical for STED scanning⁸.

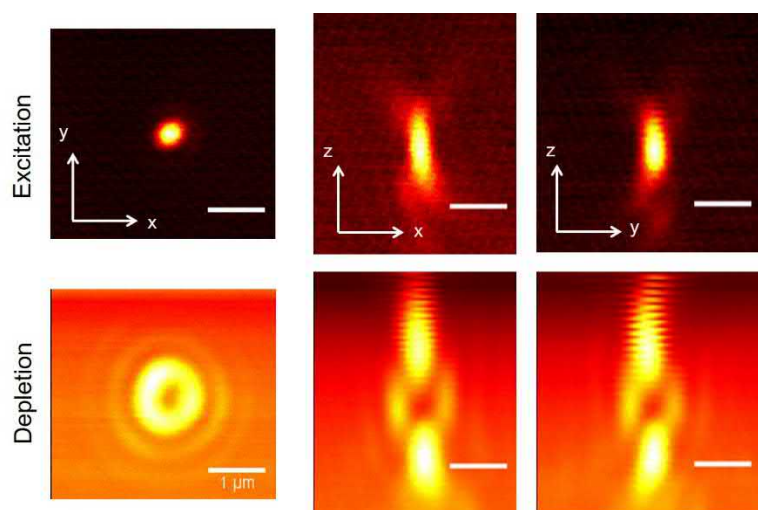


Figure S3: The beam profile of excitation laser (640 nm) (top) and 3D depletion laser (775 nm) (bottom) shown in the xy-plane (left), xz-plane (middle) and yz-plane (right). These profiles were measured using the reflection from 150 nm gold nanoparticles. Scale bars: 1 μm .

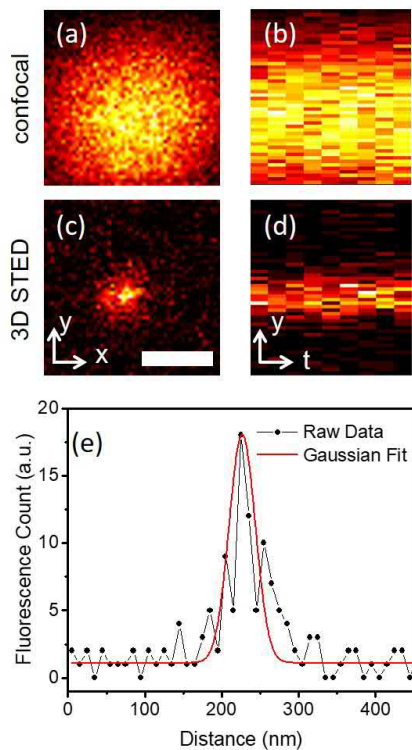


Figure S4: Confocal (a) and 3D STED (c) image of 28 nm crimson beads immobilized on a cover slip. The pixel size was set to 10 nm. The scale bar corresponds to 200 nm. Kymograph of the same crimson bead in y axis (perpendicular to membrane nanotube) for (b) confocal and (d) 3D STED scanning. Nine line scans were performed at 10 μ s pixel dwell time with 10 nm pixel size (each line scan takes 0.5 ms). (e): Gaussian fitting of the y-line scan gives 3D STED resolution to be better than 40 nm.

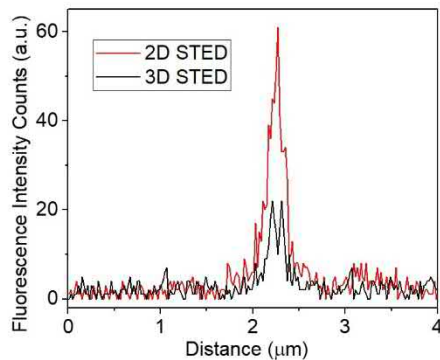


Figure S5. Intensity profile along a line scan across a membrane nanotube with 2D (red) and 3D (black) STED beams collected with pixel size of 20 nm. The 2D STED image is brighter but its effective resolution is lower due to the fluorescence signal arising from the out-of-focus part of the nanotube in z-axial direction. The signal-to-noise ratio for 3D STED is reduced but still sufficiently high (presumably because of the high quantum efficiency of the dye) to resolve the tube walls seen as peaks.

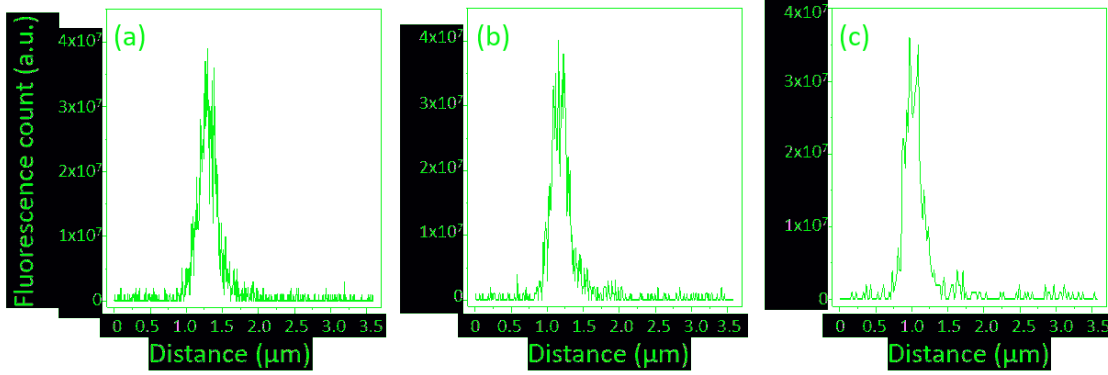


Figure S6. Line scan of a nanotube using (a) 5 nm, (b) 10 nm and (c) 20 nm pixel size. At 20 nm pixel size, the data not only becomes smoother (higher signal-to-noise ratio) but it also allows distinguishing the precise position of the two peaks indicative for the wall-crossings of the membrane nanotube.

S4 STED image analysis

To measure the tube diameter, a small image region (typically, $1 \times 1 \mu\text{m}$) including the extruded nanotube was chosen (typically in the middle of the nanotube) and 100 line scans were performed through the selected portion of the nanotube in direction perpendicular to its length (along the y-axis in Fig. 1b in the main text). The reliable and unbiased extraction of nanotube diameters was complicated by fluctuations of the nanotubes during the measurement. These fluctuations lead to a spatial displacement of the nanotube between individual scans (both in y- and z-directions, i.e. also out-of-focus), obscuring the extraction of the tube diameter. We employed an automated image analysis routine to align the individual line scans. An example of an experimentally obtained kymograph is shown in Fig. 2a in the main text. To obtain subpixel accuracy the individual line scans were linearly interpolated (interp1, MATLAB 2014a) to 0.1 pixel resolution. The individual line scans were then aligned by maximizing the overlap of the integrated intensity between two consecutive line scans l_j and l_j of length m as measured by

$$\max_{k \in \{-2m, 2m\}} \int l_{i+1}(n-k)l_i(n)dn$$

where the integral is evaluated numerically (trapz, MATLAB 2014a). The line scan l_i is shifted by the value of k at maximal overlap relative to the next lines scan with $i=i+1$. By iterating over all line scans, an aligned kymograph is obtained. As judged from the confocal image, the nanotube stays on average in focus during the measurement. The aligned line scans in the kymograph were then averaged as shown in Fig. 2d in the main text and the tube diameter determined from the distance between the two major maxima corresponding to the wall-crossing of the tube. Figure S7 shows the dependence of the measured tube diameter on the applied membrane tension of the aspirated vesicle (same data as in Fig. 3 in the main text).

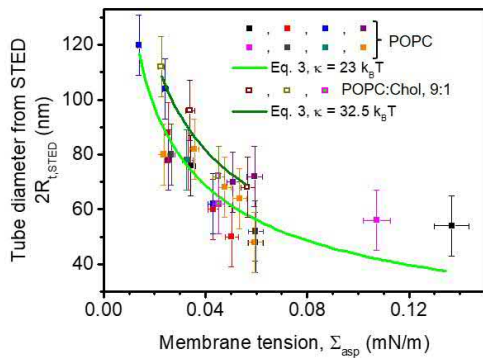


Figure S7. Plot of membrane nanotube diameter as directly measured using STED ($R_{t,STED}$) at varying membrane tension Σ_{asp} and for vesicles with two compositions – POPC (solid symbols) and POPC:Chol 9:1 (open symbols). Different colors correspond to measurements on different vesicles. The two curves show the calculated tube diameter using Eq. 3 in the main text with bending rigidity $\kappa = 23 k_B T$ as measured independently for POPC membranes, and $\kappa = 32.5 k_B T$ as assessed from literature values for membranes made of POPC:Chol 9:1.

S5 Tube pulling experiment for deducing the membrane bending rigidity

Pulling of outward membrane nanotubes from GUVs can be used to assess the membrane bending rigidity. For symmetric membranes, the pulling force is $f_t = 2\pi\sqrt{2\kappa\Sigma_{\text{asp}}} - 4\pi\kappa m - \pi\kappa/R_v$ (see main text for notations). Thus, the bending rigidity κ can be directly obtained from the slope of the dependence of the pulling force, f_t , vs. $\sqrt{\Sigma_{\text{asp}}}$ (Fig. S8). For this experiment, the trap force was measured from the displacement of the bead away from the trap center, Δx . Bright field images of the trapped bead were collected using the CCD camera at the back port of the microscope. The bead was first recorded free and then attached via a nanotube to the GUV held by a micropipette at different aspiration pressures. For each of these measurements, 100 frames were collected with 1 ms exposure time at 9 frames per second. As explained in Section S3.1, the sub-pixels bead position was determined using centroid tracking algorithm⁴. The trap force was then determined from $f_t = \kappa_{\text{tr}} \Delta x$ using the predetermined trap constant κ_{tr} .

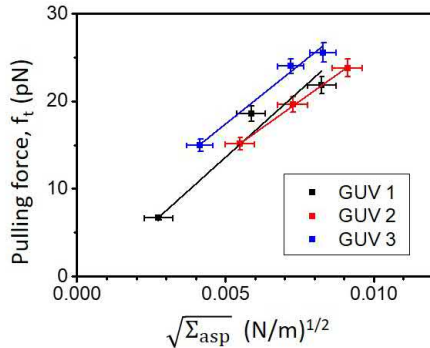


Figure S8. Pulling force versus the square root of membrane tension (Σ_{asp}) for three different GUVs. The solid lines are the linear fit for the data of the respective GUVs. The bending rigidity is found to be $\kappa = 23 \pm 5 \text{ k}_B\text{T}$.

Movie S1. Example for a fluctuating floppy vesicle suitable for micropipette aspiration (real time, 10 s at 24 frames per second). The scale bar corresponds to $10 \mu\text{m}$.

References

1. Angelova, M. I.; Dimitrov, D. S., Liposome Electroformation. *Faraday Discussions* **1986**, *81*, 303-311.
2. Dimova, R., Giant Vesicles and Their Use in Assays for Assessing Membrane Phase State, Curvature, Mechanics, and Electrical Properties. *Annu. Rev. Biophys.* **2019**, *48* (1), 93-119.
3. Gracià, R. S.; Bezlyepkina, N.; Knorr, R. L.; Lipowsky, R.; Dimova, R., Effect of cholesterol on the rigidity of saturated and unsaturated membranes: fluctuation and electrodeformation analysis of giant vesicles. *Soft Matter* **2010**, *6* (7), 1472-1482.
4. Dasgupta, R.; Verma, R. S.; Gupta, P. K., Microfluidic sorting with blinking optical traps. *Opt. Lett.* **2012**, *37* (10), 1739-1741.
5. Gelles, J.; Schnapp, B. J.; Sheetz, M. P., Tracking kinesin-driven movements with nanometre-scale precision. *Nature* **1988**, *331* (6155), 450-453.
6. Prévost, C.; Tsai, F.-C.; Bassereau, P.; Simunovic, M., Pulling Membrane Nanotubes from Giant Unilamellar Vesicles. *JoVE* **2017**, (130), e56086.
7. Sahl, S. J.; Hell, S. W.; Jakobs, S., Fluorescence nanoscopy in cell biology. *Nat. Rev. Mol. Cell Biol.* **2017**, *18*, 685.
8. Lauterbach, M. A.; Keller, J.; Schönle, A.; Kamin, D.; Westphal, V.; Rizzoli, S. O.; Hell, S. W., Comparing video-rate STED nanoscopy and confocal microscopy of living neurons. *Journal of Biophotonics* **2010**, *3* (7), 417-424.